Hindawi
Geofluids
Volume 2022, Article ID 3165524, 15 pages
https://doi.org/10.1155/2022/3165524

Research Article

Experimental Study on Grouting and Flow Characteristics of Rough Vertical Fractures

Zheng Li,[1] **Jie Liu**,[1,2,3] **Qian Shi**,[1] **Kun Mao**,[1] **Zhao Li**,[1] **Hongyu Tang**,[4] **and Tianlong Wang**[1]

[1]*College of Civil Engineering & Architecture, China Three Gorges University, Yichang 443002, China*
[2]*Key Laboratory of Geological Hazards on Three Gorges Reservoir Area, Ministry of Education, Yichang 443002, China*
[3]*Hubei Key Laboratory of Disaster Prevention and Mitigation, Yichang 443002, China*
[4]*Chengdu Xingrong Environment Co. Ltd., Chengdu 610041, China*

Correspondence should be addressed to Jie Liu; liujiea@126.com

Received 24 September 2021; Revised 27 June 2022; Accepted 23 July 2022; Published 30 August 2022

Academic Editor: Qingquan Liu

It is of great engineering significance to study the seepage characteristics and flow field distribution of rough fractured rock masses for grouting to stop leakage. Through the visual fracture seepage test device we developed, the visual seepage characteristics of tension fractures under vertical angles and different stress paths of grout and water were studied. Through silica gel secondary mould turning technology, the fracture morphology is accurately reprinted; based on GIS simulation technology, the visualization of the fracture surface spatial data is realized; the actual seepage area and flow path of the fluid are measured accurately by using digital image self-recognition technology, and the variation law of the grout and water seepage area under the coupling of normal stress and water pressure is obtained. Through visualization, it is pointed out that, with the increase of normal stress, the fracture water can be divided into three stages, archipelago flow, transition flow, and groove flow, while the grout has no capillary permeability and no archipelago flow effect because of its high viscosity. The critical point of grout antiseepage is defined and calibrated by data. Based on the analysis of the cross-sectional velocity of the groove flow, it is pointed out that the relationship between the velocity on the flow path and JRC is an exponential function. The main flow path is mainly distributed in the area where the JRC is relatively small. As the normal stress increases, the first deflection point of the grout flow path appears in the maximum region of JRC (6.42); the secondary deflection point appears in the second largest region of the flow path JRC (4.53), and the fluid of deflection point has the maximum kinetic energy on the main flow path. The current study can accurately obtain the relevant parameters of vertical fracture grouting seepage characteristics and provide theoretical guidance for solving the key scientific problems in grouting engineering, such as invisible flow paths and unmeasurable velocity vectors.

1. Introduction

Under long-term geological action, there are various roughness joints in rock mass, which are the main channels of fluid flow in rock mass and play a major role in controlling groundwater flow and migration of oil, gas, and mineral particles [1, 2]. The analysis of joint seepage is one of the hot issues in the field of rock mass seepage in recent years.

The study of cubic law extends from a smooth parallel plate model to rough fracture. On the basis of a large number of flow experiments, the cubic law of single fracture seepage is obtained [3–5]. However, there are few smooth fractures in nature, and most of them are rough fractures, which limits the applicability of the cubic law. To solve this problem, the influence of roughness is considered in many aspects, and the roughness coefficient is introduced to correct it in the cubic law [6, 7]. The Forchheimer equation can accurately describe the characteristics of nonlinear seepage flow [8]. In addition, the Navier–Stokes equations can also describe the flow law of fluids [9, 10].

The stresses have an effect on the seepage state of fractures by changing the aperture of the fracture. Because natural fractures have a limited extension length, the fracture surface is uneven, and there may be fillers, coupled with the influence of hydraulic gradients and environmental stress, leading that the real seepage law in rock mass fractures is very complex [11, 12]. On the effect of stress, Zhao et al. [13] proposed the effective stress permeability model of rough single crack, and the effective stress permeability coefficient of rough single crack is less than one. Lee and Cho [14] analyzed the hydraulic characteristics of rough fractures under the shear load. Zhou et al. [15] studied the permeability variation of rough single fracture under dynamic and static loads. The effect of stress on seepage characteristics of fractures is mainly reflected by changing the fracture aperture, so it is also necessary to consider the influence of fracture deformation caused by surrounding rock stress. Ma et al. [16] established an improved seepage model based on fractal dimension to predict permeability evolution by compression seepage test. Zhou et al. [17] studied the nonlinear flow characteristics of rough fractures at low Reynolds number under different stress states. Some studies show that aperture roughness increases three times when the normal stress increases to 50 MPa [18]. Chen et al. [19] adopted 3D rough rock fracture model to conduct seepage tests under different confining pressures, which showed the streamline becomes more tortuous and the critical Reynolds number increases under high stress. The relationship between the flow rate and fracture surface roughness under different normal stresses is also studied [20, 21].

The influence on the seepage characteristics can be attributed to two factors: the one is contact area, and the other is the tortuosity effect of the joint surface. A reduction of fracture aperture will lead to the closure of some fracture channels; the variation in the fracture aperture of joint surfaces with different roughness is not unique under the action of stress, and the aperture distribution of the fracture surface is quite different, which leads to an increase in the fracture surface contact area and the closure of a large number of seepage channels [22, 23]. The fractures with large roughness and slip degree have large seepage zone, and the residual aperture is large under low stress state. The shear displacement has no effect on the aperture size distribution of unmatched fractures [24, 25]. Sheng et al. [26] proposed a method to calculate the tortuosity index of fractal secondary fractures and described the fractal distribution of the aperture degree of secondary fractures. Some studies indicate that the standard deviation of apertures and tortuosity increase with JRC increasing [27]. In the study of the tortuous effect of rough fracture seepage, the variation of seepage flow diameter and cross-sectional area caused by the roughness of the joint plane and the uneven distribution of aperture width and the tortuous effect of seepage caused by contact between joints are studied [28]. Murata and Saito [29] analyzed the relationship between the tortuosity effect of joint seepage and fractal parameters and the contact area ratio by means of numerical experiments and laboratory tests. The evolution of natural fracture contact area during shearing shows that the change of contact area is directly related to the damage of microconvex body [30]. Xiong et al. [31] conducted a quantitative analysis of the tortuous degree of the flow channel.

In the previous seepage model experiment, because the concealment of the model medium is invisible, the specific seepage process, diffusion law, and occurrence state of the fluid in the fracture cannot be directly observed. Compared with the traditional research, the emergence of 3D printing technology provides important technical support for the establishment of real rock fracture channel model and can be used to analyze the seepage flow law in fractures [32]. Suzuki et al. [33] made smooth fracture network samples with random distribution of fracture length and inclination angle using 3D printing technology. Some researchers proposed to use acoustic emission to detect the structural shape of fractures and CT imaging to reconstruct the fracture network model, but it has some limitations and cannot observe the flow of fluid in fractures. The others proposed the method of X-ray image digital radiography to observe the flow of fluid in the fracture [34, 35]. In addition, some researchers used NMRI technology to observe fluid flow in fractures or to explore the flow pattern of fluid by analyzing more than 300 SEM images [36–39]. Although these methods have some visual effects, they are expensive and have some limitations. Moreover, there are still some difficulties in accurately describing the flow process in rough fractures [40, 41].

Due to the characteristics of fuzziness, concealment, randomness, and complexity of grouting engineering, there is insufficient understanding of grouting diffusion and predictive control, and the grouting theory lags behind the engineering practice. It is necessary to study the diffusion law of grout (seepage area, seepage velocity, and seepage path) in the process of grouting, which can provide reference for the design and construction of grouting engineering and promote the scientific, controllable, and fine grouting technology. In this paper, through the accurate reprinting technique of silica gel secondary mould turning, the morphology of natural rock fractures are accurately replicated. Using the visual seepage test device, combined with digital image self-recognition technology and GIS three-dimensional image drawing of fracture surfaces, the effects of tensile vertical fracture roughness, water pressure and normal stress on the seepage path, seepage area, seepage velocity, and other parameters are studied, which provides a theoretical basis for the disaster control of water inrush and mud inrush in the project.

2. Materials and Methods

2.1. Test Scheme of Fracture Seepage. The existing tunnel engineering and underground engineering construction process are unloading construction process, and the seepage phenomenon in multiple spatial angles exists in rock fractures. Therefore, this study adopts unloading test scheme with normal stress ranging from 0.6 to 0.1 MPa and water pressure increasing from 0.1 to 0.6 MPa and selects fracture angle of 90° to carry out the test, as shown in Table 1. The variation of seepage velocity, seepage area, and seepage path width under the influence of different normal stress and water pressure is studied. The test process is shown in Figure 1.

Table 1: Test design of sample loading.

(σ_f, σ_s)		Water pressure σ_s (MPa)					
		0.1	0.2	0.3	0.4	0.5	0.6
Normal stress σ_f (MPa)	0.6	(0.6,0.1)	(0.6,0.2)	(0.6,0.3)	(0.6,0.4)	(0.6,0.5)	(0.6,0.6)
	0.5	(0.5,0.1)	(0.5,0.2)	(0.5,0.3)	(0.5,0.4)	(0.5,0.5)	(0.5,0.6)
	0.4	(0.4,0.1)	(0.4,0.2)	(0.4,0.3)	(0.4,0.4)	(0.4,0.5)	(0.4,0.6)
	0.3	(0.3,0.1)	(0.3,0.2)	(0.3,0.3)	(0.3,0.4)	(0.3,0.5)	(0.3,0.6)
	0.2	(0.2,0.1)	(0.2,0.2)	(0.2,0.3)	(0.2,0.4)	(0.2,0.5)	(0.2,0.6)
	0.1	(0.1,0.1)	(0.1,0.2)	(0.1,0.3)	(0.1,0.4)	(0.1,0.5)	(0.1,0.6)

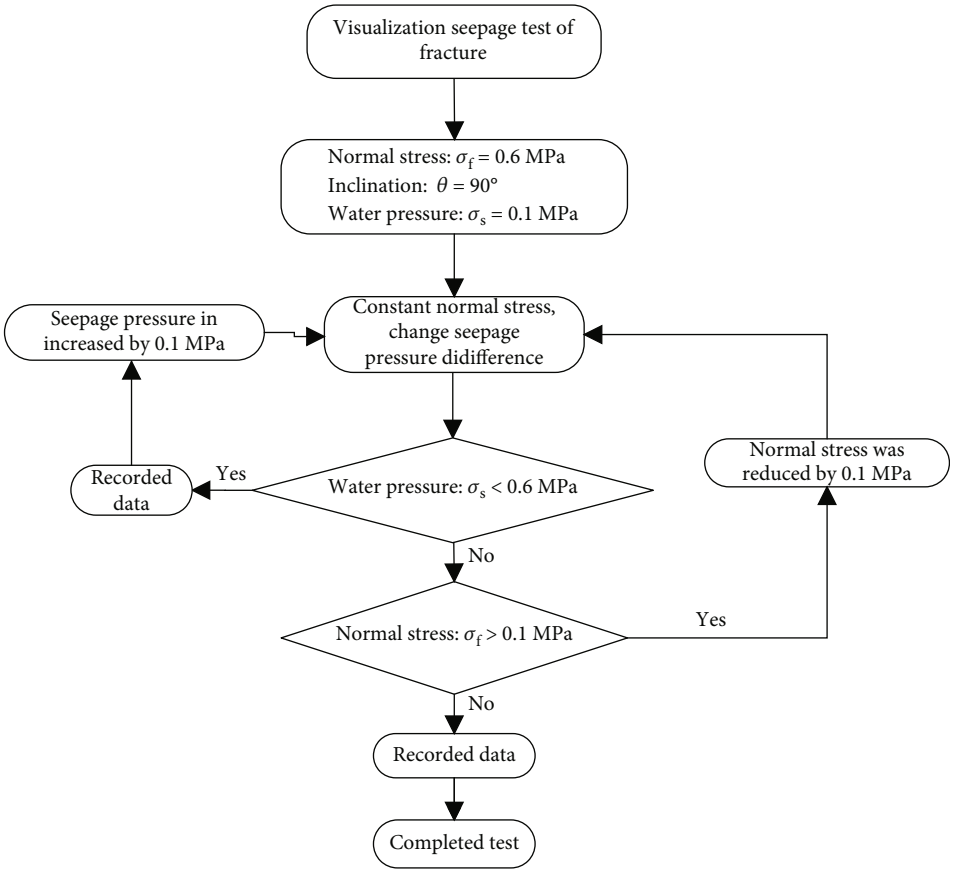

Figure 1: Flow chart of test process.

2.2. The Production of Visual Fracture Model

2.2.1. Specimen Preparations. The cubic rock sample is selected from the sandstone in the water-level-fluctuation zone of Zigui County in the Three Gorges Reservoir area. The particle size of detrital material in the rock ranges from 0.1 mm to 0.3 mm, and the particle size of sand is mainly 0.15 mm to 0.2 mm, belonging to medium-fine sandstone. Using calcium oxide and calcium sulfoaluminate as the expansion components of the composite expansion agent, v-shaped groove depth of 3~5 cm, groove width of 5 cm, and groove bottom shoulder-oriented perpendicular to the ground facilitate the crack through. The surface was bonded with epoxy resin AB glue, and two fractures were obtained to completely coincide with rock sample A and B. Then, the sample was cut into cuboids with a size of 200 mm × 200 mm × 50 mm by a rock-cutting machine.

2.2.2. The Proposal of Accurate Reprinting Technology for Silica Gel Secondary Remoulding. The K39 resin material easily bonds with the rock interface, which leads to the inability to remove the rock surface, while the silica gel texture is relatively soft and does not bond with the natural rock and the K39 resin, which can clearly depict the grains of the rock fracture surface. Firstly, silica gel is poured into the tensioned rock fracture surface to reproduce the rock fracture

morphology. The resin material is then poured into the surface of silica gel engraved with rock fracture morphology. After the K39 transparent resin material is fully hardened, the fracture morphology (Figure 2) corresponding to rock sample A (or rock sample B) is accurately reproduced on the resin material after it has been fully hardened at room temperature for 2 to 3 days. To ensure that the deformation modulus of the K39 transparent rock material is consistent with that of the raw rock, the K39 transparent resin material is prepared with reference to an average elastic modulus of 0.67 GPa of natural rock: accelerator content of 0.8%, hardener content of 0.6%, and defoamer content of 0.6%.

2.3. Experimental Device. As show in Figure 3, the fracture visualization seepage device is mainly composed of four parts: seepage device, angle adjustment device, data monitoring equipment, and loading device. K39 transparent resin has the advantages of good fluidity, high transparency, and good hardness after curing. While accurately reproducing the roughness of rock fractures, it can also achieve the visualized effect and accurately measure the seepage area and path from the microscopic perspective under the coupling of multiple factors such as the multiangle water gravity effect in the space of water pressure and normal stress pressure. The function of seepage flow and other related parameters provides the basis for accurately obtaining the related parameters of rock seepage characteristics.

Apply normal stress to rock fractures by pressurized air cushion and reaction frame. The pressurized air cushion exerts normal stress on the bottom of rock sample through balloon expansion, and at the same time, the air cushion also plays a role of homogenizing the stress on the bottom of rock sample. The reverse force of the upper counter force frame is applied to the transparent acrylic plate, and the acrylic plate can play the role of homogenizing the force on the upper and lower rock samples, so as to ensure the uniform load on the surface of the upper and lower rock samples. The grout with water cement ratio of 2 : 1 flows into the fracture from the left water injection chamber.

2.4. Arc GIS 3D Image Drawing of Fracture Surface. The technology of GIS can be used for storing and processing by scanning, measurement, and numerical expression to obtain spatial data and generate a variety of new spatial information according to the measured data to realize the visualization of spatial data. The data were obtained by 3D scanning and imported into GIS software. The TIN is established from vector data, and the three-dimensional map of rock fracture surface is obtained by TIN to DEM, as shown in Figure 4. Furthermore, the fracture surface roughness can be clearly observed by enhanced tensile treatment.

2.5. Calculation of Seepage Area. As shown in Figure 5, the experimental image (a) is processed with black and white highlights to obtain image (b), which is then superimposed by the solid colour layer to obtain image (c). In image (c), the black area is the fracture water-invaded wet area, and the red area is the dry area of no water-invaded area. The image resolution is checked in the Image software, the total number

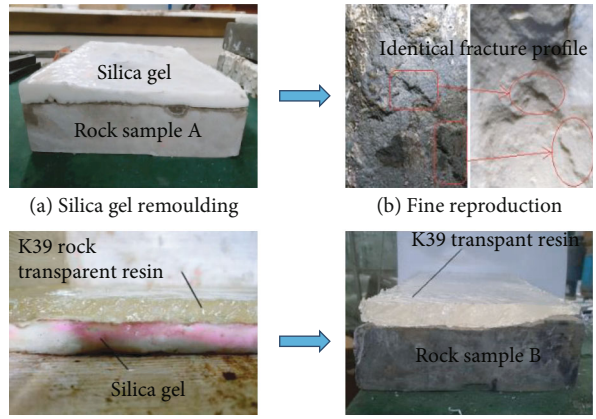

(a) Silica gel remoulding
(b) Fine reproduction
(c) K39 transparent resin secondary mould turning
(d) K39 visual rock sample

Figure 2: Accurate reprinting of original rock grain by silica gel remoulding.

Figure 3: Diagram of the visual test device for fracture seepage. Picture of the experimental device. 1, test framework; 2, high-speed camera; 3, high-pressure pipe; 4, gas cylinder; 5, antiforce frame; 6, transparent resin; 7, motor test pump; 8, pressurized air cushion; 9, angle-adjusting instrument; 10, flow meter.

of pixels in the fracture water area is extracted, and the actual horizontal seepage area A (unit: cm^2) is calculated by

$$A = \frac{P}{R^2} \times 2.54^2, \quad (1)$$

where P is the pixels and R (unit: ppi) is the resolution.

3. Variation in the Seepage Area of Fracture Water and Grout under Different Stress Paths Based on Visualization

3.1. The Relationship between Seepage Area S-Water Pressure σ_s-Normal Stress σ_f. The seepage area distribution under different water pressures is shown in Figure 6:

The seepage area of water and grout under different stress paths is calculated by a digital image area self-recognition technique. Figure 7 shows the relationship among the actual seepage area, water pressure, and the normal stress of fracture water and grout under different stress paths.

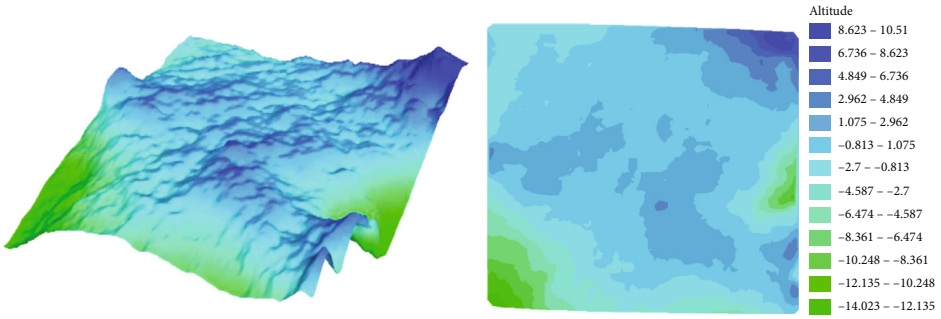

Figure 4: Three-dimensional map of rock surface.

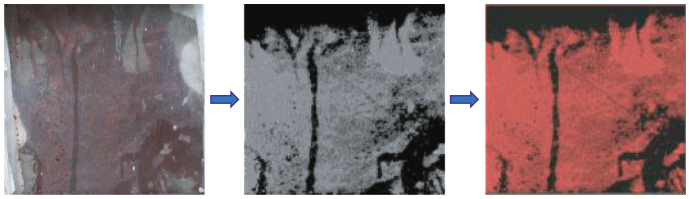

(a) Original image (b) Black and white highlight processing (c) Mixed processing

Figure 5: Image processing.

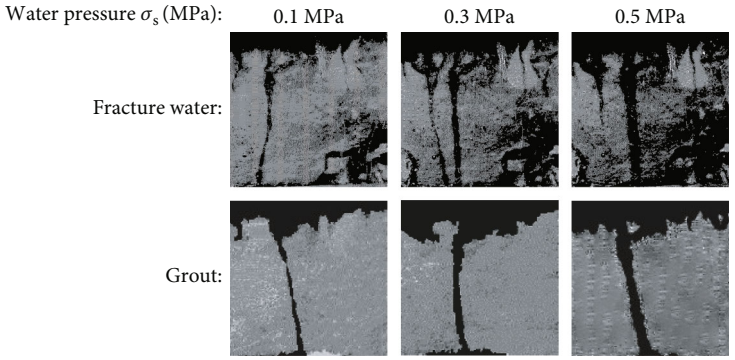

Figure 6: Black-and-white highlighted binary image.

According to the fitting data, when the normal stress is constant, the seepage area increases linearly with the water pressure.

$$A_{ij1} = k_1\sigma_{s1} + a_1, \tag{2}$$

$$A_{ij2} = k_2\sigma_{s2} + a_2. \tag{3}$$

In the formula, i represents the i-th normal stress; j represents the j-th water pressure; A_{ij} represents the horizontal projected diffusion area (cm^2) of fracture water seepage; σ_s is water pressure (MPa); k is the influence rate of water pressure on seepage area, and a is the seepage area (cm^2) affected by gravity under the condition of no water pressure.

3.2. The Relationship between the Influence Rate of Seepage Area k and the Normal Stress σ_f. According to the slope of the horizontal projection diffusion area curve of water pressure and fracture seepage in Figure 7, the relationship between normal stress and the curve slope is established, which characterizes the coupling relationship between normal stress and the water pressure of water and grout, respectively, as shown in Figure 8.

With normal stress increasing, the influence rate of the seepage area decreases gradually. The λ_1 is defined as the influence rate of k_1 of the seepage area of fracture water and the slope of the normal stress relation curve, λ_2 is the influence rate k_2 of the seepage area of the grout and the slope of the normal stress curve, and the relationship is as follows:

(1) There is a linear decreasing relationship between the influence rate k_1 of the seepage area and the normal stress of the fracture water.

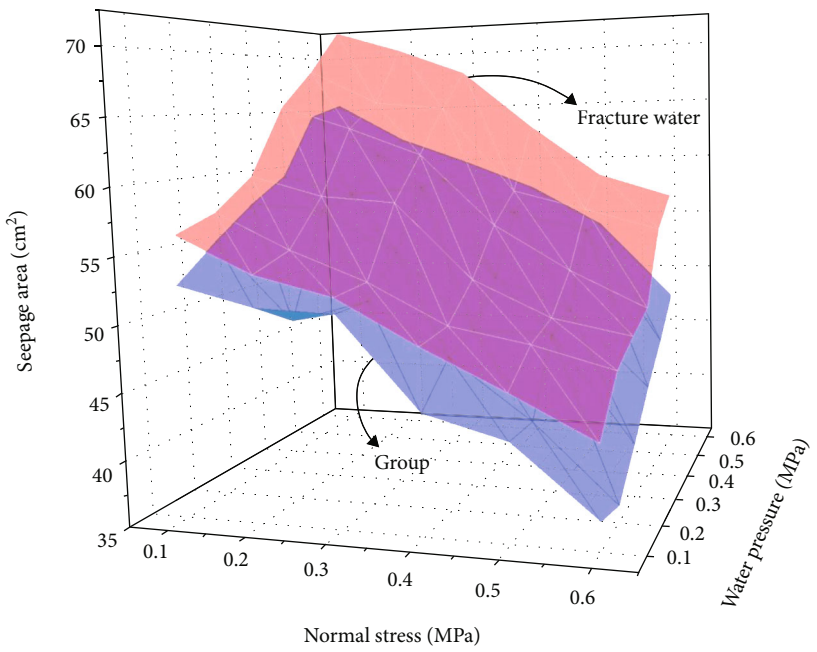

Figure 7: Relationship between seepage area and water pressure and normal stress.

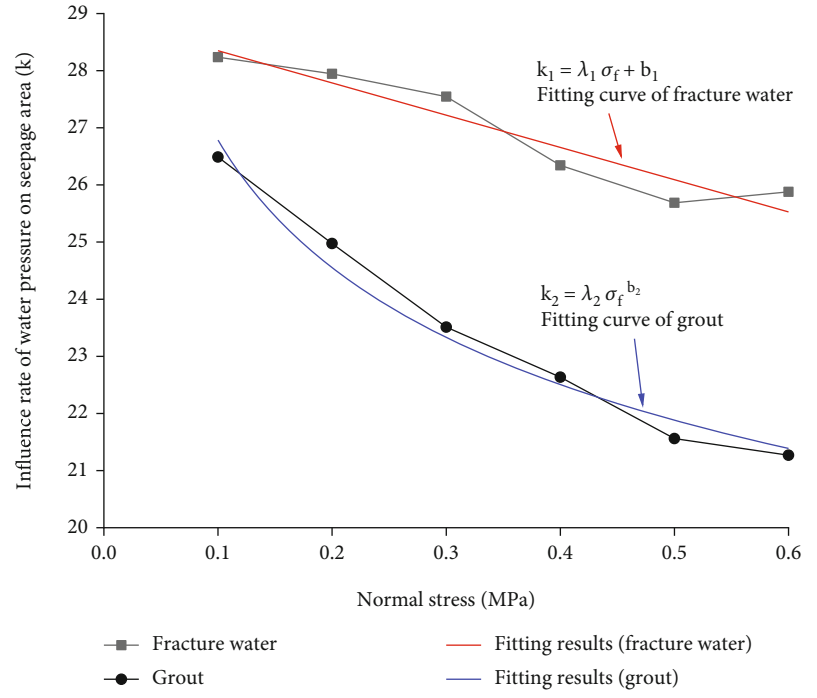

Figure 8: Relationship between slope and normal stress.

$$k_1 = -5.65\sigma_f + 28.92,\ R^2 = 0.913 \quad (4)$$

$$k_2 = 20.06 \cdot \sigma_f^{-0.13},\quad R^2 = 0.896 \quad (5)$$

(2) There is a power function decreasing relationship between the influence rate k_2 of the seepage area and the normal stress.

By substituting Formula (6) into Formula (2) and Formula (7) into Formula (3), the variation formulas of the seepage area of fracture water and grout under the coupling action of σ_f and σ_s are obtained as follows:

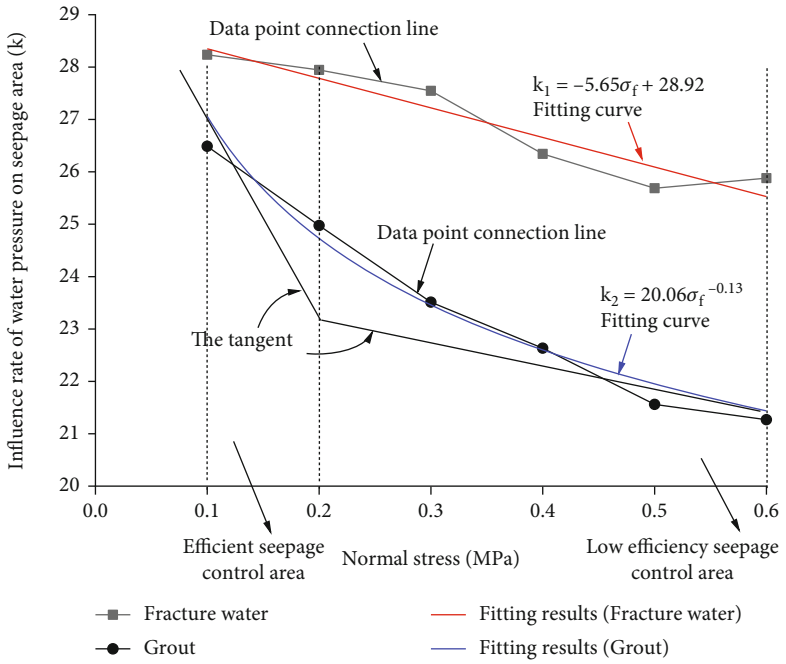

Figure 9: Relationship between the influence rate of the seepage area and normal stress.

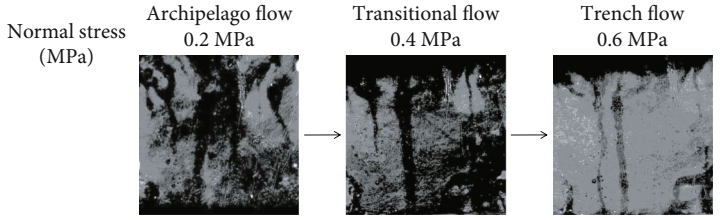

Figure 10: Flow state change under different normal stresses.

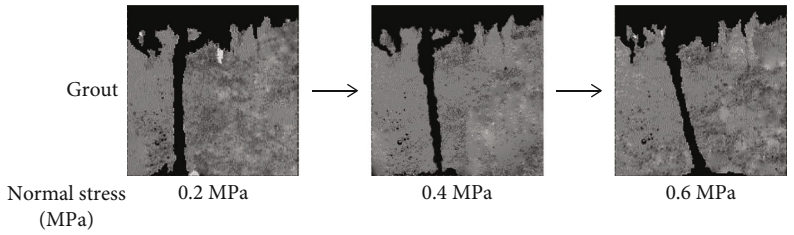

Figure 11: Grout flow path diagram.

$$A_{ij1} = \left(-5.65\sigma_f + 28.92\right)\sigma_s + a_1, \tag{6}$$

$$A_{ij2} = \left(20.06{\sigma_f}^{-0.13}\right)\sigma_s + a_2. \tag{7}$$

3.3. Definition and Calibration of the Critical Point of the Imperviousness of Grout. To accurately locate the relationship between normal stress and grout antiseepage, the critical point of each section is calibrated, and an objective calibration method is proposed to determine the critical point. The tangents at normal stresses of 0.1 MPa and 0.6 MPa are drawn, and the coordinates of the critical points are determined according to the intersection of the two tangent equations, as shown in Figure 9.

Tangent equation under normal stress of 0.1 MPa is

$$k - k_{\sigma_{f_1}} = \lambda_2 \cdot b \cdot {\sigma_{f_1}}^{b-1}\left(\sigma_f - \sigma_{f_1}\right). \tag{8}$$

Tangent equation under normal stress of 0.6 MPa is

$$k - k_{\sigma_{f_6}} = \lambda_2 \cdot b \cdot {\sigma_{f_6}}^{b-1}\left(\sigma_f - \sigma_{f_6}\right). \tag{9}$$

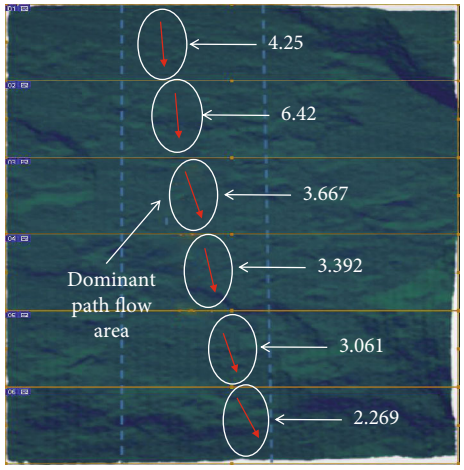

Figure 12: Rock surface scan image and JRC value.

Then, the point of intersection (σ_f, k_{ij}) of the two tangent equations is as follows.

$$\begin{cases} \sigma_f = \dfrac{\lambda_2 \cdot b\sigma_{f_1}{}^{b} - \lambda_2 \cdot b\sigma_{f_6}{}^{b} - k_{\sigma_{f_1}} + k_{\sigma_{f_6}}}{\lambda_2 \cdot b\sigma_{f_1}{}^{b-1} - \lambda_2 \cdot b\sigma_{f_6}{}^{b-1}}, \\ k = \dfrac{k_{\sigma_{f_1}}\sigma_{f_6}{}^{b-1} - k_{\sigma_{f_6}}\sigma_{f_1}{}^{b-1} + \lambda_2 \cdot b\sigma_{f_1}{}^{b-1}\sigma_{f_6}{}^{b} - \lambda_2 \cdot b\sigma_{f_1}{}^{b}\sigma_{f_6}{}^{b-1}}{\sigma_{f_6}{}^{b-1} - \sigma_{f_1}{}^{b-1}}. \end{cases} \tag{10}$$

The solution is as follows:

$$\begin{aligned} \sigma_f &= 0.208, \\ k &= 23.257. \end{aligned} \tag{11}$$

The relationship between the influence rate of the seepage area and normal stress under unit water pressure is as follows: the left side of the critical point (0~0.208 MPa) is the scope where the influence rate of seepage area changes with the high speed of normal stress, and the change on the right side (0.208~0.6 MPa) is slow. That is, when $\sigma_f < 0.208$ MPa, the fracture surface has fewer contact points and less contact stiffness, so the fracture closes quickly. The effect of preventing seepage is obvious, and the efficiency is high, which is defined as a high-efficiency preventing seepage area; when $\sigma_f > 0.208$ MPa, the contact points increase, the contact stiffness increases, the fracture closing speed slows down, and the natural flow capacity of the fracture decreases gradually. The influence rate of the seepage area changes slowly, and the effect of preventing seepage is not obvious, which makes it a low-efficiency preventing seepage area.

Therefore, the above method can guide the construction of the seepage control scheme to reduce the migration of fracture fluid in antiseepage applications such as nuclear waste and water conservancy projects.

3.4. Distribution Law of Fracture Water Seepage Area S. When the normal stress increases, the seepage area and equivalent aperture change, as shown in Figure 10. In the initial stage, the normal stress is relatively small, the fracture surface is in point contact, and the flow state is similar to the archipelago flow distribution. In the transitional flow stage, the change rate is the largest, the contact area of the fracture surface increases gradually, a large number of seepage channels are closed, and the seepage area decreases. When the normal stress is greater than 0.4 MPa, the width of the flow path decreases, there are only one or two mainstream paths, the flow path is groove flow, and the influence rate of normal stress on the seepage area decreases.

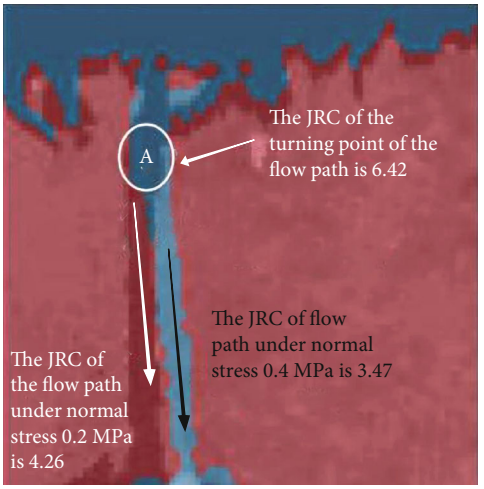

Figure 13: Superposition of the flow path diagram normal stress between 0.4 MPa and 0.6 MPa.

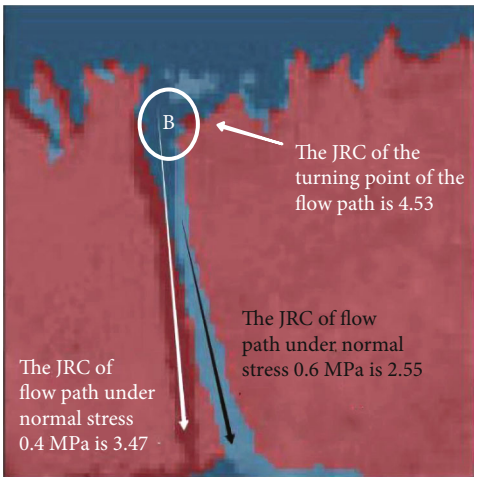

Figure 14: Superposition of the flow path diagram under normal stress between 0.4 MPa and 0.6 MPa.

3.5. Distribution Law of Grout Seepage Area S. A high-speed camera was used to record the evolution process of flow path with the increase of normal stress. The video was divided into frames, and the images before and after the flow path deflecting were overlapped to analyze the evolution law of flow path trajectory.

3.5.1. Variation of Flow Path Distribution. The flow path of fracture water changes from multiple to one, while the flow

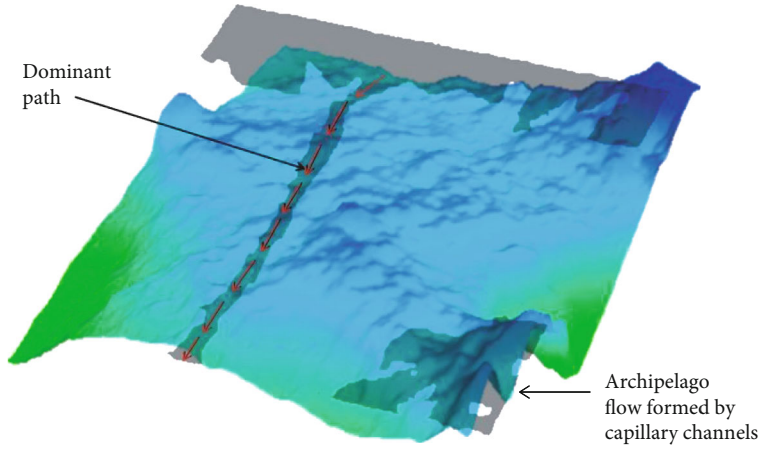

Figure 15: Superposition of the fracture water flow path and 3D diagram.

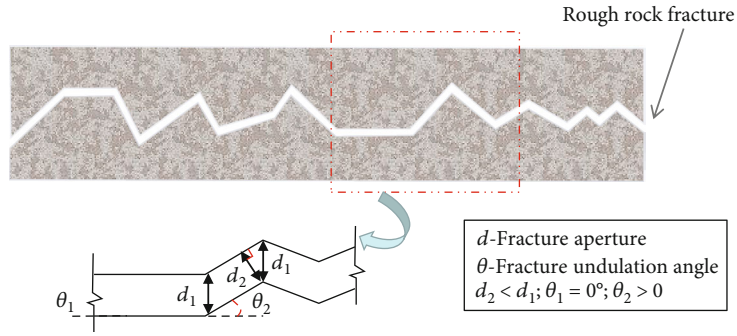

Figure 16: Schematic diagram of the change in rough fracture aperture.

path of grout is relatively single, and there is no archipelago effect. Because of the small size of water molecules, the capillary effect can be formed in the capillary channel in the fracture, and there is a small seepage channel, which is also the reason for the formation of the archipelago flow effect.

Due to the viscosity coefficient of the grout is larger than that of water, a filtration effect will be formed near the originally closed channel to block the capillary channel. Therefore, as shown in Figure 11, the main flow path is the main seepage channel in the process of grout flow.

3.5.2. JRC Value Calculation. The joint roughness coefficient (JRC) is used to characterize the fracture flow path roughness, and the empirical formula proposed by Tse is used to calculate the fracture JRC value:

$$Z_2 = \left[\frac{1}{M(\Delta x)^2}\sum_{i=1}^{M}(Z_{i+1} - Z_i)^2\right]^{1/2}, \quad (12)$$

$$\mathrm{JRC} = 32.2 + 32.47 \lg Z_2, \quad (13)$$

where Z_2 is the root mean square of the slope, Δx is the distance between two adjacent sampling points, $Z_{i+1} - Z_i$ is the height difference between two adjacent sampling points in the Z direction, and M is the total number of sampling intervals.

The 3D data of the cross-sectional area is extracted through Arc GIS, and the JRC value on the flow path is calculated, as shown in Figure 12:

3.5.3. Analysis of Flow Path Deflection. From the view of the fracture surface roughness, as shown in Figure 13, when the normal stress increases from 0.2 MPa to 0.4 MPa, through the layer superposition, it is found that the grout flow path begins to deflect in the A region where the flow path roughness is the highest and where JRC is 6.42. As shown in Figure 14, when the normal stress increases from 0.4 MPa to 0.6 MPa, region B is on the flow path where the roughness secondary point and JRC are 4.53. When the normal stress increases, the fracture channels in regions A and B are closed successively, and the grout cannot pass through this area, which leads to the deflection of the flow path.

From the perspective of energy, through the flow path velocity change in Chapter 4.2, we can see that, in region A, where the flow velocity surges and the average growth rate is 96%, the kinetic energy of the grout is the largest and most prone to deflection.

3.6. Analysis of the Influence of the Change of Aperture on the Change of Groove Flow Area

3.6.1. Three-Dimensional Image Superposition of Flow Path and Fracture. By using the layer superposition method, the

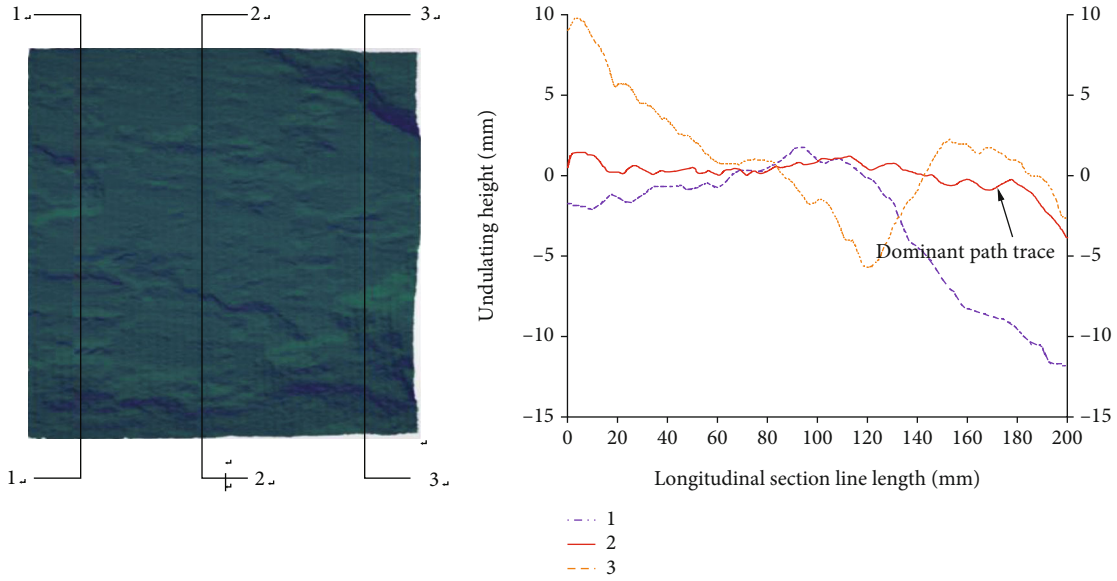

(a) Schematic diagram of section line

(b) Height value of section line undulation

Figure 17: Variation of undulating height of profile.

visual fracture water flow path map is superimposed with the three-dimensional figure of the fracture surface, as shown in Figure 15. By adjusting the transparency of the fracture water, it can be seen that the dominant path flow area is mainly distributed in the middle area with low fluctuation in the three-dimensional map. The fracture water will form the archipelago flow through the capillary channel, but the grout does not exhibit this phenomenon.

3.6.2. Analysis of JRC and Aperture Variation. Ideally, the two fracture surfaces can completely match, as shown in Figure 16. In the process of vertical upwards translation d_1 distance of the upper fracture surface, the change of aperture of the fracture surface with an undulating inclination angle of $\theta = 0$ is d_1, and for the inclined fracture $\theta > 0$, the aperture between the two fracture surfaces is d_2, as shown in Figure 16. According to the relationship of mathematical geometry, $d_1 > d_2$. In theory, the aperture should be small for places with higher fluctuations. In Figure 15, it can be seen that the main seepage channel is distributed in the range of low roughness.

As can be seen in Figure 17(b), the three profile curves are plotted. The JRC for profile curve 1 is 10.41, for profile 2 is 3.84, and for profile 3 is 13.67. The absolute values of $H_{Z1} = 13.547$, $H_{Z2} = 4.492$, and $H_{Z3} = 15.63$ and the slope root mean square (RMS) are $\triangle Z_1 = 0.213$, $\triangle Z_2 = 0.134$, and $\triangle Z_3 = 0.269$, respectively. Among them, the absolute value of the root mean square and elevation of the 2-section slope is the smallest, which corresponds to the area of mainstream diameter, which confirms once again that the aperture of the area with a large value of JRC is small.

Therefore, when the normal stress increases, the seepage channel in the region with large roughness closes first. At the same time, the seepage area of the fracture surface decreases, and the main flow path shrinks with normal stress increasing.

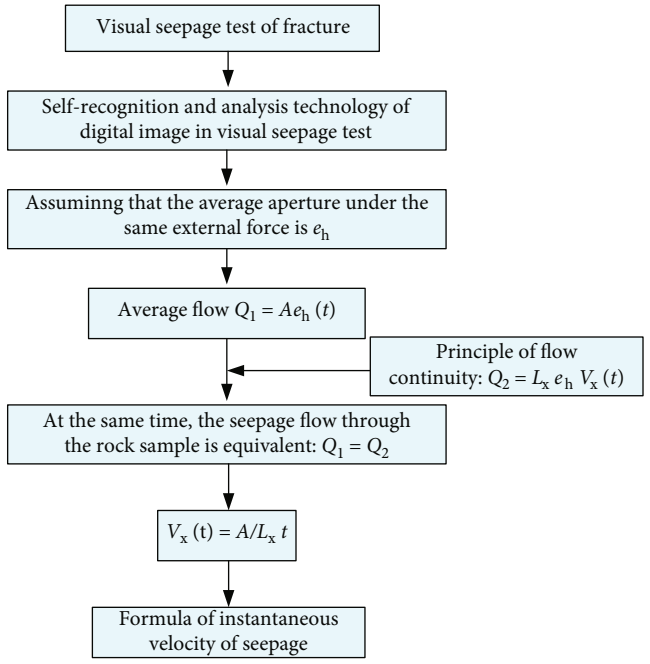

Figure 18: Flow chart of instantaneous velocity derivation.

4. Analysis of Cross Section Velocity of Groove Flow Based on Digital Image Processing

The dynamic velocity of water has an important effect on grout diffusion. The study of the flow velocity is of guiding significance for grouting engineering.

4.1. Establishment of Instantaneous Velocity Formula of Seepage. As shown in Figure 18, the t is the flow time from the inlet to the outlet under the main seepage path. The A (unit: cm^2) is the seepage area; the Q_2 (cm^3/s) is flow rate

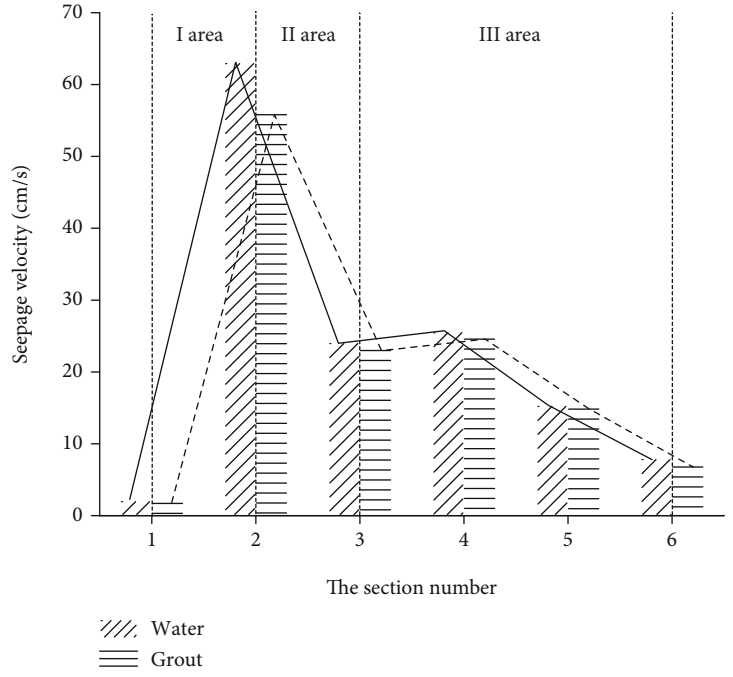

Figure 19: Velocity relationship of each section under 0.1 MPa water pressure.

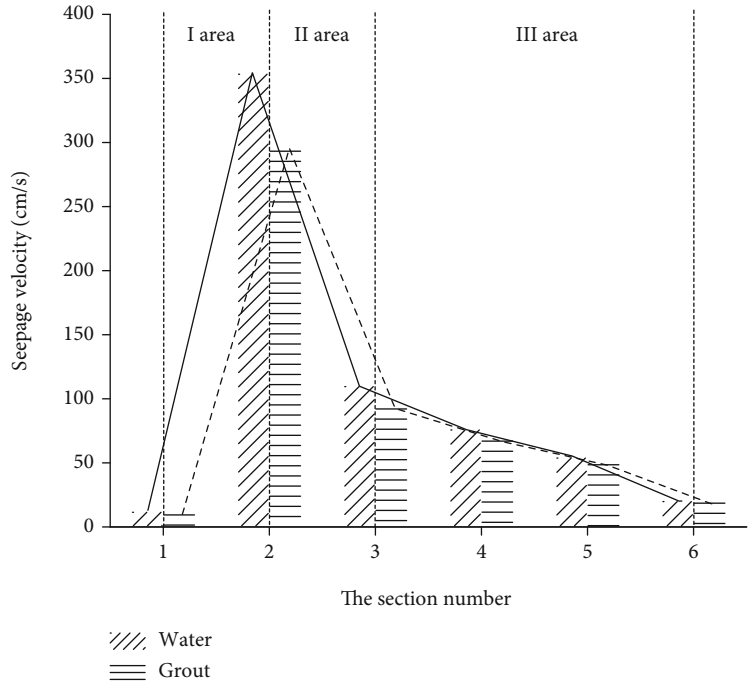

Figure 20: Velocity relationship of each section under 0.6 MPa water pressure.

of the X section; the $v_x(t)$ (cm/s) is the flow velocity under the X section and is a function of t; the L (cm) is the cross section width of the X section.

The computing method of the cross section width L is as follows.

(1) The image is divided into six equal parts and the five cross sections are selected from the inlet

(2) The coordinates of the two ends of the seepage path are obtained in the Image software information window, and then, the width of the cross section can be obtained by subtracting the two transverse coordinates (X coordinates)

4.2. Comparison of Seepage Velocity of Fracture Water and Grout on Different Sections. According to the test results,

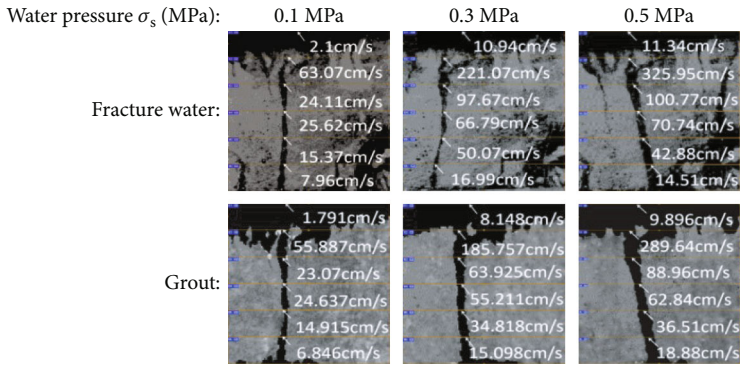

Figure 21: Rates on the path of water and grout flow.

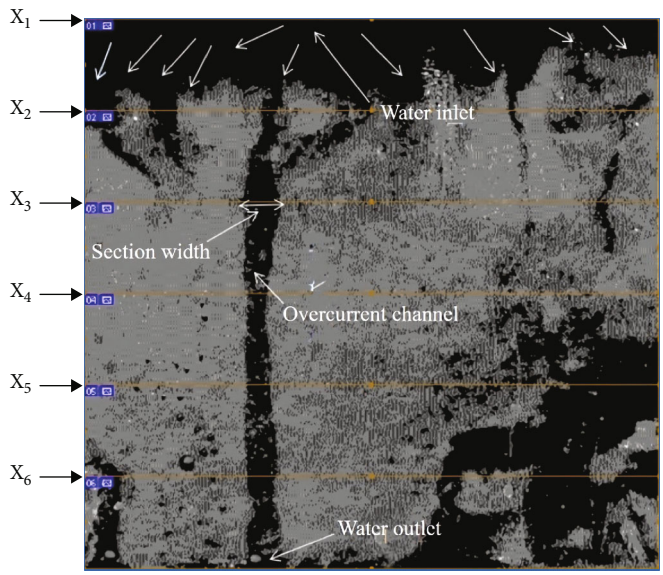

Figure 22: Image section division and aperture acquisition.

the flow velocity of cross section is calculated by the formula, which is shown in Figures 19 and 20.

As show in Figure 19, when the normal stress is 0.1 MPa, the flow velocity of fracture water and grout show obvious stage characteristics in different sections. We divided it into three regions, namely, I (1–2 sections), II (2–3 sections), and III (3–6 sections). Among them, the area I is of the surge zone; the area II is of the steep drop zone, and the area III is the uniform descending zone.

(1) In the surge zone, because the width of flow path of section 1 is the largest (200 mm), the flow velocity is the smallest. In section 2, the width of the flow path decreases sharply, and the flow velocity increases sharply

(2) In the steep drop zone, the flow velocity decreases rapidly. When the water pressure is 0.1 MPa, the decreasing ratio of fracture water velocity is 61.77% and that of grout velocity is 58.72%. When the water pressure is 0.6 MPa, the decreasing ratio of water velocity is 68.5% and that of grout velocity is 66.31%. Therefore, the decrease of flow velocity in this area is the largest, and the required grouting pressure is small

(3) In the uniform descending zone, the rate of fracture water and grout decrease gently, and the head loss in this zone is relatively small

4.3. Correspondence Analysis of Visual Flow Path Velocity Change and JRC. In order to further intuitively express the velocity distribution of water and grout in rock fractures, the velocity of each section on the rock surface is shown in Figure 21 when the normal stress is 0.1 MPa and the water pressure varies from 0.1 MPa to 0.5 MPa.

Figure 22 shows that the width of cross section 1 is equal to the width of fracture surface w (200 mm), and its velocity (8.96 cm/s) is the smallest compared to all the sections, but the seepage area of this section is the largest. The value of JRC in the area of section 2 is the largest, and the width of the cross section of the flow path decreases sharply. It can be inferred from the formula of Figure 18 that the velocity

Table 2: Velocity of water and grout in different JRC regions on the flow path.

Section serial number		1	2	3	4	5	6
Cross-sectional velocity v (cm/s)	Water	8.96	231.357	81.775	61.475	38.103	16.575
	Grout	11.109	199.332	67.253	53.145	31.769	15.154
Cross-sectional area JRC		1.32	6.42	3.667	3.392	3.061	1.85

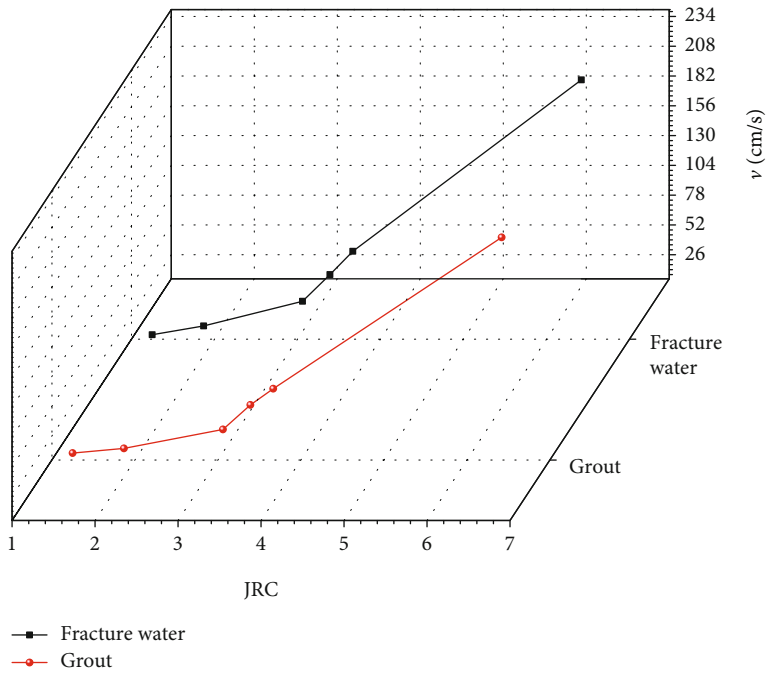

Figure 23: Relationship between cross-sectional velocity and JRC.

of this section is also the largest in the whole flow path. Table 2 and Figure 23 show that the velocity increases with increasing JRC because the aperture of the area with large JRC value is small, the flow channel becomes narrow, and the velocity v increases at the same flow rate. For grouting in fractures with large roughness, the grouting velocity can be increased by increasing the grouting pressure to resist dynamic water velocity. For smoother fractures with the same aperture, a good effect of preventing seepage can be achieved by lower grouting pressure.

5. Conclusion

(1) Through the fracture visual seepage test device we developed, the visual seepage characteristics of rough fractures under vertical angles and different stress paths of grout and fracture water are tested; the fracture morphology is accurately reprinted by using silicone secondary mould reetching technology. Based on GIS simulation technology and longitudinal tensile enhancement processing according to the measured data, the visualization of fracture surface spatial data is realized

(2) Based on visual digital image self-recognition technology, the actual seepage area and flow diameter of the fluid are finely measured, and there is a linear relationship between the seepage area and the water pressure. The influence rate k of the water pressure on the seepage area decreases linearly with normal stress increasing, while the grout shows a power function relationship because of the larger viscosity coefficient than water

(3) With normal stress increasing, the first deflection point of the grout flow path appears in the maximum region of JRC (6.42). The secondary deflection point appears in the secondary region of the flow path JRC (4.53), and the deflection point is the point of maximum kinetic energy on the flow path. Because of its high viscosity, there is no capillary permeability; there is no archipelago effect, and the critical point of grout seepage is defined

(4) Based on the analysis of the cross-sectional velocity of the groove flow based on digital image processing, it is pointed out that the relationship between the velocity on the flow path and JRC is an exponential

function; the fracture aperture is larger in the area with small roughness, and the main flow path is mainly distributed in the area with small JRC. The study of the cross-sectional velocity of the flow path is of guiding significance for local energy loss, grout diffusion, and the selection of reasonable grouting pressure

Data Availability

The research data are included within the article, and further data are available from the corresponding author upon request.

Conflicts of Interest

The authors declare that there are no conflicts of interest regarding the publication of this article.

Acknowledgments

This work was supported by the National Natural Science Foundation of China (52079071 and 51979151); Open Fund of the Key Laboratory of Geological Hazards in the Three Gorges Reservoir Region, Ministry of Education (2020 KDZ08); Guangxi Key Laboratory of Geotechnical Mechanics and Engineering Open Fund (20-Y-KF-02); Hubei Provincial Natural Science Foundation General Project (2020CFB584); and Research Fund for Excellent Dissertation of China Three Gorges University (2021BSPY016 and 2021SSPY025).

References

[1] Y. F. Chen, J. M. Hong, H. K. Zheng, Y. Li, R. Hu, and C. B. Zhou, "Evaluation of groundwater leakage into a drainage tunnel in Jinping-I arch dam foundation in southwestern China: a case study," *Rock Mechanics and Rock Engineering*, vol. 49, no. 3, pp. 961–979, 2016.

[2] D. Ma, H. Duan, W. Liu, X. Ma, and M. Tao, "Water–sediment two-phase flow inrush hazard in rock fractures of overburden strata during coal mining," *Mine Water and the Environment*, vol. 39, no. 2, pp. 308–319, 2020.

[3] G. M. Lomize, *Flow in Fractured Rocks*, State Press, Moscow, 1951.

[4] C. Louis and Y. N. Maini, "Determination of in-situ hydraulic parameters in jointed rock," *International Society of Rock Mechanics, Proceedings*, vol. 1, pp. 1–19, 1970.

[5] D. T. Snow, "Anisotropie permeability of fractured media," *Water Resources Research*, vol. 5, no. 6, pp. 1273–1289, 1969.

[6] M. O. Kottwitz, A. A. Popov, T. S. Baumann, and B. J. P. Kaus, "The hydraulic efficiency of single fractures: correcting the cubic law parameterization for self-affine surface roughness and fracture closure," *Solid Earth*, vol. 11, no. 3, pp. 947–957, 2020.

[7] X. He, M. Sinan, H. Kwak, and H. Hoteit, "A corrected cubic law for single-phase laminar flow through rough-walled fractures," *Advances in Water Resources*, vol. 154, p. 103984, 2021.

[8] C. C. Xia, X. Qian, P. Lin, W. M. Xiao, and Y. Gui, "Experimental investigation of nonlinear flow characteristics of real rock joints under different contact conditions," *Journal of Hydraulic Engineering*, vol. 143, no. 3, pp. 1–14, 2017.

[9] S. H. Lee and K. K. Yeo, "Assessment of the validity of Stokes and Reynolds equations for fluid flow through a rough-walled fracture with flow imaging," *Geophysical Research Letters*, vol. 41, no. 13, pp. 4578–4585, 2014.

[10] R. C. Liu, B. Li, and Y. J. Jiang, "Critical hydraulic gradient for nonlinear flow through rock fracture networks: the roles of aperture, surface roughness, and number of intersections," *Advances in Water Resources*, vol. 88, pp. 53–65, 2016.

[11] Y. Chen, H. Lian, W. Liang, J. Yang, V. P. Nguyen, and S. P. A. Bordas, "The influence of fracture geometry variation on non-Darcy flow in fractures under confining stresses," *International Journal of Rock Mechanics and Mining Sciences*, vol. 113, pp. 59–71, 2019.

[12] J. Q. Zhou, L. Wang, C. Li, H. Tang, and L. Wang, "Effect of fluid slippage on eddy growth and non-Darcian flow in rock fractures," *Journal of Hydrology*, vol. 581, pp. 124440–124444, 2020.

[13] Z. Zhao, S. Chen, Y. Chen, and Q. Yang, "On the effective stress coefficient of single rough rock fractures," *International Journal of Rock Mechanics and Mining Sciences*, vol. 137, pp. 104556–104558, 2021.

[14] H. S. Lee and T. F. Cho, "Hydraulic characteristics of rough fractures in linear flow under normal and shear load," *Rock Mechanics and Rock Engineering*, vol. 35, no. 4, pp. 299–318, 2002.

[15] Z. Zhou, J. Zhang, X. Cai, S. Wang, X. du, and H. Zang, "Permeability experiment of fractured rock with rough surfaces under different stress conditions," *Geofluids*, vol. 2020, 15 pages, 2020.

[16] D. Ma, J. Zhang, H. Duan et al., "Reutilization of gangue wastes in underground backfilling mining: overburden aquifer protection," *Chemosphere*, vol. 264, p. 128400, 2021.

[17] J. Q. Zhou, S. H. Hu, S. Fang, Y. F. Chen, and C. B. Zhou, "Nonlinear flow behavior at low Reynolds numbers through rough-walled fractures subjected to normal compressive loading," *International Journal of Rock Mechanics and Mining Sciences*, vol. 80, pp. 202–218, 2015.

[18] H. Javanmard, A. Ebigbo, S. D. C. Walsh, M. O. Saar, and D. Vogler, "No-flow fraction (NFF) permeability model for rough fractures under normal stress," *Water Resources Research*, vol. 57, no. 3, pp. 1–18, 2021.

[19] Y. Chen, A. P. S. Selvadurai, and Z. Zhao, "Modeling of flow characteristics in 3D rough rock fracture with geometry changes under confining stresses," *Computers and Geotechnics*, vol. 130, pp. 103910–103920, 2021.

[20] T. Babadagli, X. Ren, and K. Develi, "Effects of fractal surface roughness and lithology on single and multiphase flow in a single fracture: an experimental investigation," *International Journal of Multiphase Flow*, vol. 68, pp. 40–58, 2015.

[21] G. Rong, L. Cheng, R. He, J. Quan, and J. Tan, "Investigation of critical non-linear flow behavior for fractures with different degrees of fractal roughness," *Computers and Geotechnics*, vol. 133, p. 104065, 2021.

[22] J. L. Shao, Q. Zhang, W. B. Sun, Z. Y. Wang, and X. X. Zhu, "Numerical simulation on non-Darcy flow in a single rock fracture domain inverted by digital images," *Geofluids*, vol. 2020, 13 pages, 2020.

[23] N. Huang, R. C. Liu, Y. J. Jiang, B. Li, and L. Y. Yu, "Effects of fracture surface roughness and shear displacement on geometrical and hydraulic properties of three-dimensional crossed

rock fracture models," *Advances in Water Resources*, vol. 113, pp. 30–40, 2018.

[24] C. Lu, Y. Luo, J. Guo et al., "Numerical investigation of unpropped fracture closure process in shale based on 3D simulation of fracture surface," *Journal of Petroleum Science and Engineering*, vol. 208, p. 109299, 2022.

[25] A. Cardona, T. Finkbeiner, and J. C. Santamarina, "Natural rock fractures: from aperture to fluid flow," *Rock Mechanics and Rock Engineering*, vol. 54, no. 11, pp. 5827–5844, 2021.

[26] G. L. Sheng, Y. L. Su, and W. D. Wang, "A new fractal approach for describing induced-fracture porosity/permeability/ compressibility in stimulated unconventional reservoirs," *Journal of Petroleum Science and Engineering*, vol. 179, pp. 855–866, 2019.

[27] Z. Mahdi, S. Serkan, T. Wendy, and H. Bruce, "Linear flow behaviour of matched joints–case study on standard JRC profiles," *Geomechanics and Geoengineering*, vol. 11, no. 3, pp. 189–200, 2016.

[28] A. M. Cook, L. R. Myer, N. G. W. Cook, and F. M. Doyle, "The effect of tortuosity on flow through a natural fracture," *Proceedings of the 31st U.S. Symposium*, Rock Mechanics: Contributions and Challenges, Jun 18-20, Golden, CO, USA, 1990.

[29] S. Murata and T. Saito, "Estimation of tortuosity of fluid flow through a single fracture," *Journal of Canadian Petroleum Technology*, vol. 42, no. 12, pp. 39–45, 2003.

[30] M. A. Pirzada, M. Bahaaddini, O. Moradian, and H. Roshan, "Evolution of contact area and aperture during the shearing process of natural rock fractures," *Engineering Geology*, vol. 291, p. 106236, 2021.

[31] F. Xiong, Q. Jiang, Z. Ye, and X. Zhang, "Nonlinear flow behavior through rough-walled rock fractures: the effect of contact area," *Computers and Geotechnics*, vol. 102, pp. 179–195, 2018.

[32] Y. Ju, H. Xie, Z. Zheng et al., "Visualization of the complex structure and stress field inside rock by means of 3D printing technology," *Chinese Science Bulletin*, vol. 59, no. 36, pp. 5354–5365, 2014.

[33] A. Suzuki, N. Watanabe, K. Li, and R. N. Horne, "Fracture network created by 3-D printer and its validation using CT images," *Water Resources Research*, vol. 53, no. 7, pp. 6330–6339, 2017.

[34] H. Sun, X. Liu, Z. Ye, and E. Wang, "A new proposed method for observing fluid in rock fractures using enhanced x-ray images from digital radiography," *Geomechanics and Geophysics for Geo-Energy and Geo-Resources*, vol. 8, no. 1, pp. 1–16, 2022.

[35] H. L. Ramandi, M. A. Pirzada, S. Saydam, C. Arns, and H. Roshan, "Digital and experimental rock analysis of proppant injection into naturally fractured coal," *Fuel*, vol. 286, p. 119368, 2021.

[36] K. Du, X. Li, M. Tao, and S. Wang, "Experimental study on acoustic emission (AE) characteristics and crack classification during rock fracture in several basic lab tests," *International Journal of Rock Mechanics and Mining Sciences*, vol. 133, pp. 104411–104415, 2020.

[37] A. Fheed, K. Kłodowski, and A. Krzyżak, "Fracture orientation and fluid flow direction recognition in carbonates using diffusion-weighted nuclear magnetic resonance imaging: an example from Permian," *Journal of Applied Geophysics*, vol. 174, p. 103964, 2020.

[38] Z. J. Wu, K. Lu, L. Weng et al., "Investigations on the seepage characteristics of fractured sandstone based on NMR real-time imaging," *Chinese Journal of Rock Mechanics and Engineering*, vol. 40, no. 2, pp. 263–275, 2021.

[39] N. Golsanami, M. N. Jayasuriya, W. Yan et al., "Characterizing clay textures and their impact on the reservoir using deep learning and Lattice-Boltzmann simulation applied to SEM images," *Energy*, vol. 240, p. 122599, 2022.

[40] Y. D. Chen, W. G. Liang, H. J. Lian, J. F. Yang, and V. P. Nguyen, "Experimental study on the effect of fracture geometric characteristics on the permeability in deformable rough-walled fractures," *International Journal of Rock Mechanics and Mining Sciences*, vol. 98, pp. 121–140, 2017.

[41] W. Cui, X. Zou, Z. Li, Z. Jiang, and W. Xie, "Seepage diffusion in a fractal single micro-rock-fracture under multiple experimental cases," *Rock and Soil Mechanics*, vol. 41, no. 1, pp. 1–10, 2020.